Journal of Low Temperature Physics (2026) 222:122
https://doi.org/10.1007/s10909-026-03455-y

Effects of Lanthanum Doping on Structural Evolution, Morphological Features, and Flux Pinning in $FeSe_{0.5}Te_{0.5}$ Single Crystals with Machine Learning Assistance

Jie Zhang[1,2] · Jian Peng[1] · Jens Hänisch[3] · Shengnan Zhang[4] · Shunpeng Shi[1] · Chuanyu Zhang[1] · Fanggong Cai[5] · Guo Yan[6] · Yong Zhao[7]

Received: 14 May 2026 / Accepted: 23 July 2026

Abstract
Single crystals of $La_xFe_{1-x}Se_{0.5}Te_{0.5}$ ($x = 0$, 0.02, 0.04, 0.06, 0.08) were grown using the self-flux method. A systematic investigation of the effects of La addition revealed changes in the lattice parameters, with the lattice parameter a decreasing and the lattice parameter c showing a slight increasing tendency. The superconducting transition temperature showed no significant dependence on La doping. However, when x reached 0.04, the critical current density derived from magnetization loops using the Bean model increased. The dominant pinning mechanism induced by La in $FeSe_{0.5}Te_{0.5}$ was identified as normal point pinning at low magnetic fields. At the same time, machine learning was employed to quantitatively model the composition–property relationship between La doping and superconducting and magnetic properties; the results indicate that this method is effective in capturing experimental trends. This work demonstrates that rare earth doping could be a viable strategy for optimizing flux pinning in iron-based superconductors.

Keywords $FeSe_{0.5}Te_{0.5}$ · La addition · Flux pinning · Machine learning · Superconductivity

1 Introduction

With the continuous development of data-driven methodologies, machine learning (ML) is increasingly applied as a complementary tool to support and enhance experimental investigations [1]. By modeling experimental data, ML approaches can predict material properties using smaller datasets, thereby reducing the need for extensive repetitive experiments [2]. For superconducting systems, where physical properties exhibit high sensitivity to stoichiometric ratios, traditional experimental optimization often demands substantial time and cost [3]. Therefore, integrating machine learning methods with experimental research offers a novel approach for

Extended author information available on the last page of the article

Published online: 10 August 2026

optimizing and understanding superconducting properties in these systems. In this study, a Gaussian regression model was used to validate the experimental results. In 2008, the FeSe superconductor garnered considerable interest owing to its simple crystal structure and low toxicity [4]. Shortly thereafter, Fang et al. reported that partial replacement of Se with Te could increase the superconducting transition temperature (T_c) from 8 to 14 K [5]. Furthermore, T_c can also be enhanced to 27 K under high pressure (1.48 GPa) [6, 7]. The superconductivity of Fe(Se,Te) is highly sensitive to stoichiometry, especially to the excess of Fe [8, 9]. The commonly used chemical approach to modify both the structural and electronic properties of the superconducting state involves substituting elements at the Fe and Se sites with others that possess different ionic radii. Substitution of anions in Fe(Se,Te) has been shown to control T_c. These substitutions suggest that the improvement in superconductivity originates from the compressed lattice, or the so-called chemical pressure [5, 10]. Doping different elements into the Fe(Se,Te) superconductor provides a means to control superconductivity. Transition metals such as Co [11], Ni [12], Cr, Mn [13], Zn, Cu [14], Nb [15], and Pd [16] replacing Fe as well as Fe off-stoichiometry have been widely investigated [17]. This typically results in a significant decrease in the critical temperature and ultimately leads to the loss of superconductivity. On the other hand, doping with other elements like B on the Se/Te site [18], or Pr [19], Li [20], Gd [21], K [22], and F [23] on the Fe site enhances the superconducting properties. Except for Pr [15] and Gd [21], doping with rare earths has not been investigated much so far, and there are no reports on La doping, which is the topic of this study.

Lanthanum (La), a rare earth element, exists mostly in the form of La^{3+}, which has the largest ionic radius among the rare earths of 1.03 Å. Therefore, when introduced into Fe(Se,Te), it is expected to induce substantial lattice distortion. This work evaluates the influence of La addition on crystal growth evolution and superconducting behavior in $FeSe_{0.5}Te_{0.5}$ single crystals.

In this work, $La_xFe_{1-x}Se_{0.5}Te_{0.5}$($x = 0$, 0.02, 0.04, 0.06, 0.08) single crystals were synthesized using a self-flux technique, and their superconducting properties were systematically investigated. The results indicate that La incorporation suppresses the superconducting transition temperature, whereas the $x = 0.04$ sample exhibits the highest critical current density, exceeding 10^4 A/cm^2 at 6 K under 6 T. A discussion on the flux-pinning mechanism in La-doped samples is provided within the framework of the Dew-Hughes model. By modeling experimental data, machine learning methods can predict material properties using smaller datasets. Comparing these predictions with the experimental results shows good consistency between the GPR analysis and the experimental observations [24]. Therefore, combining machine learning with experimental investigations provides an effective auxiliary strategy for clarifying property evolution and guiding performance enhancement in Fe(Se,Te)-based materials.

2 Methods

2.1 Sample Preparation and Measurement

Stoichiometric amounts of Fe (99.99%), Se (99.999%), Te (99.999%), and La (99%, Sigma-Aldrich) precursor powders were prepared in a nitrogen-protected glove box according to the nominal formula Fe:Se:Te:La = $1-x$:0.50:0.50:x (x = 0, 0.02, 0.04, 0.06, 0.08).The mixed powders were then pressed into pellets with a diameter of 10 mm and a thickness of 1.0 mm under a uniaxial pressure of 8 MPa. These pellets were sealed in vacuum quartz tubes. Subsequently, they were heated to 1090 °C and maintained at this temperature for 24 h. The samples were then gradually cooled to 650 °C at 2.5 °C/h, followed by oven cooling for another 12 h until room temperature was reached. The resulting samples were labeled according to the nominal La content: undoped, 0.02 La, 0.04 La, 0.06 La, and 0.08 La.

The crystallinity of the samples was characterized by X-ray diffraction ($\lambda = 1.5418$ Å) with θ–2θ scans from 10 to 70° using a PANalytical X'Pert diffractometer at room temperature. Surface morphology was observed using a field-emission scanning electron microscope (FESEM, JSM-7800F), while resistivity measurements were taken using the standard four-probe method in a Quantum Design Physical Property Measurement System (PPMS).

2.2 Gaussian Regression Model

To quantitatively establish the composition–property relationship between La doping levels and superconducting and magnetic properties, Gaussian process regression (GPR) was used to model the experimental data [25]. GPR is a nonparametric Bayesian regression method that represents the unknown mapping between input variables and output responses as a Gaussian process [26]. Consequently, it not only provides a predicted mean for the target property but also quantifies the prediction uncertainty simultaneously, which is particularly important for systems with limited experimental data. The underlying approach aligns with the standard GPR mathematical framework described in the literature. La doping concentration x is used as the input variable, while the superconducting transition temperature T_c and the magnetic susceptibility M at 6 K serve as the output targets. For T_c data, multiple measurements from each doped sample were averaged before being used for regression modeling; for magnetic susceptibility data, experimental measurements at the corresponding doping levels were directly used for training. According to the model specifications, the regression for T_c employs a squared exponential kernel function, while the regression for magnetic susceptibility uses an ARD squared exponential kernel function; both models incorporate a noise term, and the input data are standardized to minimize the impact of different units on the correlation of the kernel functions [27]. Subsequently, dense prediction points were generated across the continuous doping range to obtain a smooth GPR prediction curve and its uncertainty interval. Considering the limited number of experimentally synthesized

La-doped compositions, the GPR model was employed primarily as a machine learning-assisted analytical tool rather than a stand-alone predictive framework [28]. To provide broader compositional and structural context, superconducting composition–property information from the SuperCon database and crystallographic information from the Materials Project database were used as supporting references [29, 30]. Therefore, the objective of the GPR analysis in this work is to identify composition-dependent trends, quantify prediction uncertainty, and assist in the interpretation of experimental observations within the investigated compositional range.

The fundamental formulation of GPR is given by [31]

$$f(x) \sim \mathcal{GP}(m(x), k(x, x')) \tag{1}$$

Here, *m(x)* denotes the mean function, whereas *k (x, x')* represents the covariance kernel. The covariance kernel describes the correlation between different input points and governs the smoothness of the predictive function, as well as information propagation within the input space. For a training dataset X and observed values y, the posterior predictive distribution at the test point x_* can be expressed as [32]

$$f_* \Big| \mathbf{y} \sim \mathcal{N}(\mu_*, \sigma_*^2) \tag{2}$$

The mean and variance of the forecast are

$$\mu_* = K_*^T (K + \sigma_n^2 I)^{-1} \mathbf{y} \tag{3}$$

$$\mu_* = K_*^T (K + \sigma_n^2 I)^{-1} \mathbf{y} \tag{4}$$

Here, K denotes the covariance matrix of the training samples, K_* represents the covariance matrix between the training and test points, and σ^2 corresponds to the noise variance. Consequently, the model is able to provide a prediction along with a corresponding estimate of uncertainty.

To evaluate the model's performance, the coefficient of determination (R^2) and root mean square error (RMSE) were used as evaluation metrics, as follows:

$$R^2 = 1 - \frac{\sum_{i=1}^{n} (y_i - \hat{y}_i)^2}{\sum_{i=1}^{n} (y_i - \bar{y})^2} \tag{5}$$

$$\mathrm{RMSE} = \sqrt{\frac{1}{n} \sum_{i=1}^{n} (y_i - \hat{y}_i)^2} \tag{6}$$

Here, y_i denotes the experimental value, $\hat{y}_i$ corresponds to the predicted value, $\bar{y}$ indicates the mean of the experimental values, and n represents the sample size. The prediction uncertainty is characterized by a confidence interval; for the magnetic susceptibility model, the 95% confidence interval is written as

$$\hat{y} \pm 1.96\sigma_* \tag{7}$$

Parameter modulation: Based on the experimental measurements, a machine learning dataset was constructed for La-doped $FeSe_{0.5}Te_{0.5}$, and Gaussian process regression (GPR) was employed to establish the composition–property relationship. The La concentration x was used as the input variable, while the superconducting transition temperature T_c and the magnetization at 6 K (MMM) were taken as the output targets. Prior to training, repeated measurements were averaged and the input data were standardized to improve the predictive stability of the model for the small dataset.

3 Results and Discussions

To further illustrate the relationship between the experimental data and model analysis in this paper, a data-driven analysis workflow based on Gaussian process regression (GPR) is presented in Fig. 1. This workflow integrates experimental variables, sample preparation, and performance characterization with GPR modeling to enable the prediction of target performance and the assessment of uncertainty. Additionally, the model output results can serve as a reference for subsequent experimental range screening and parameter optimization, thereby supporting the quantitative analysis of T_c and magnetic susceptibility under La doping.

Based on the data-driven analysis framework shown in Fig. 1, predictions for the superconducting transition temperature T_c and magnetic susceptibility at 6 K under La doping were further obtained, as presented in Fig. 2. Figure 2a shows that T_c generally tends to decrease with increasing La content, with slight fluctuations observed in the intermediate doping range, suggesting a potentially nonlinear response of superconducting behavior to La doping. The corresponding $R^2 = 0.8433$ and RMSE = 0.2350 indicate that the model can reasonably describe the overall evolution of T_c, although some deviations still exist in local regions. In contrast, the magnetic susceptibility in Fig. 2b exhibits a more pronounced non-monotonic variation; its $R^2 = 0.9635$ and RMSE = 0.0008 indicate that the model has higher consistency and reliability in fitting and predicting the magnetic response. Figure 2 not only provides specific prediction results for the composition–property relationship under La doping but also further validates the effectiveness of the analysis workflow in Fig. 1 in revealing the correlation between La doping and superconducting and magnetic properties.

Building on the GPR prediction results for T_c and magnetic susceptibility shown in Figs. 2, 3 further illustrates the relationship between prediction error and the Gaussian Reliance Index (GRI). It can be observed that as the prediction error increases, the GRI generally decreases, suggesting a close relationship between model reliability and predictive accuracy. These findings indicate that the GPR model can not only capture trends in performance parameters under La doping but also provide a quantitative evaluation of prediction reliability.

To further validate the reliability of the GPR-predicted composition–property relationship, the experimentally prepared samples were subsequently characterized

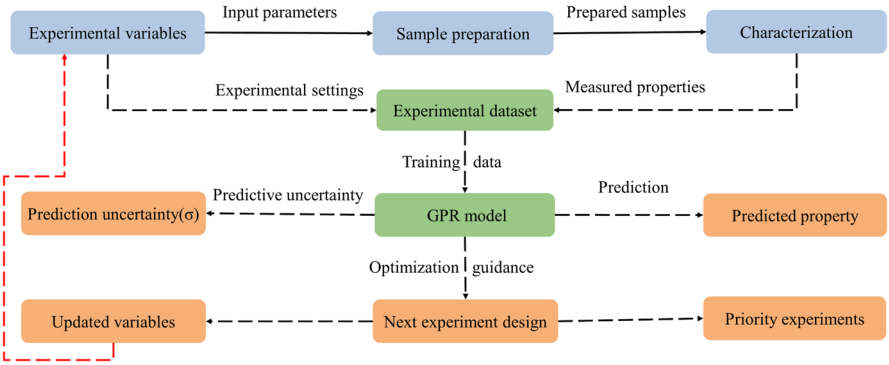

Fig. 1 Schematic illustration of the GPR-assisted closed-loop workflow for experimental design, property prediction, and optimization

in terms of their structural and physical properties. Room-temperature X-ray diffraction (XRD) patterns obtained from the bright surfaces of all single crystals, as shown in Fig. 4a, display only (00 *l*) reflections, suggesting preferential crystal growth along the *c*-axis. In addition, the La-doped $FeSe_{0.5}Te_{0.5}$ single crystals exhibit a tetragonal crystal structure with the space group *P4/*nmm [33] just as the undoped sample. Figure 4b presents the powder diffraction patterns for the different La contents, which show no evidence of secondary phases, suggesting that the samples are relatively pure and possess good crystal quality. Furthermore, the (001) rocking curve of the 0.02 La sample was measured exemplarily to investigate the out-of-plane crystalline quality (Fig. 4c). The main peak has a full width at half maximum (FWHM) of 0.46°. At a closer look, it consists of five peaks with even lower FWHM (0.11°···0.32°), which is explained by several sharply textured platelets just weakly connected and slightly tilted. [34]. Figure 4d presents the crystal lattice parameters of the sample series. As La content increases, the lattice parameter *a* decreases at relatively low doping levels and then approaches a more stable value, while the lattice parameter c shows a slight upward tendency. According to Shannon's ionic radii, La^{3+} possesses an effective ionic radius of approximately 1.16 Å, which is significantly larger than the corresponding value of approximately 0.78 Å for Fe^{2+} [35–37]. This size difference indicates that direct substitution of Fe^{2+} by La^{3+} is not strongly supported by the lattice parameter evolution. The anisotropic changes in *a* and *c* suggest that La addition affects the local structural environment of $FeSe_{0.5}Te_{0.5}$ rather than producing a uniform lattice expansion or contraction. Together with the EDS-observed compositional variation, the results indicate that La addition may involve local structural distortion, defect-related modification, compositional redistribution, and/or minor La–Se/La–Te-related species below the detection limit of XRD.

Fracture morphology of the La-doped samples is presented in Fig. 5, where characteristic lamellar structures are observed across all samples. The pure $FeSe_{0.5}Te_{0.5}$ single crystal in Fig. 5a and the 0.02 La sample in Fig. 5b exhibit layered structures with smooth impurity-free surfaces. However, with increasing La content, defects begin to

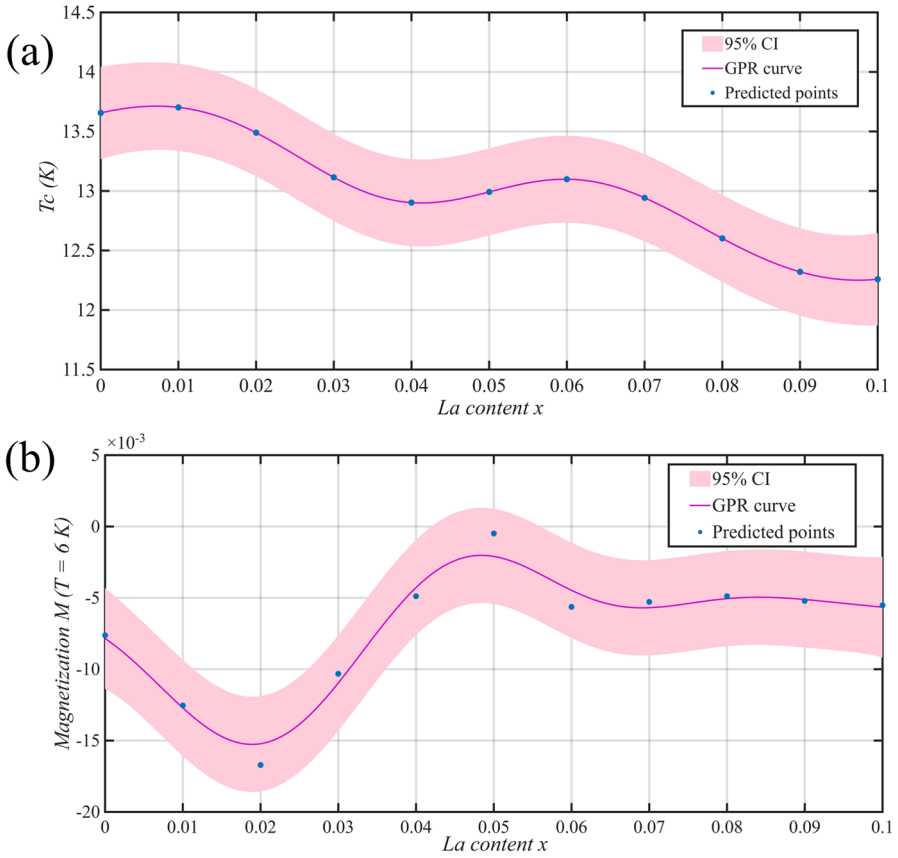

Fig. 2 GPR-predicted composition–property relationships of **a** superconducting transition temperature Tc and **b** magnetization at 6 K as a function of La content

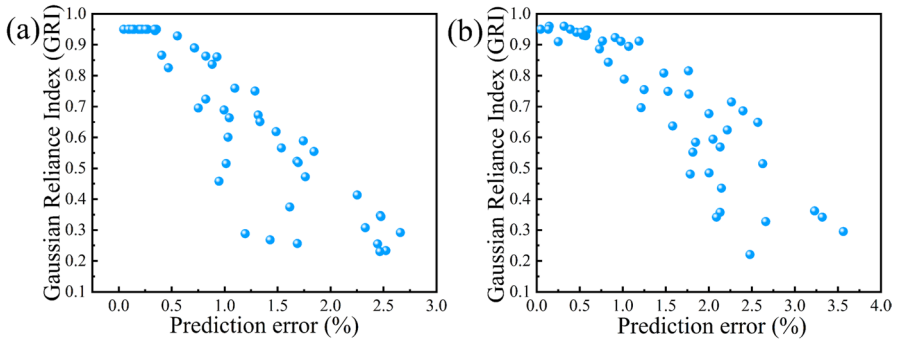

Fig.3 Comparison between experimental and Gaussian process regression (GPR) predicted values. **a** Predicted T_c versus experimental T_c. **b** Predicted magnetization M versus experimental M

emerge in the samples. Numerous spherical particles are observed on the lamellar surfaces of the 0.04 La sample in Fig. 5c. These particles are nanoscale defects similar to previous reports [18]. Figure 5d depicts a regular square structure characterized by a layered configuration for the 0.06 La sample with clear 001 and 101 facets.

The morphology of the 0.08 La sample (Fig. 5e) shows debris at the steps, resulting in an uneven surface. As the La doping level increases, defects begin to appear and proliferate within the crystal, suggesting that excessive La doping in Fe(Se,Te) may negatively affect the crystal quality. This may be associated with increased structural degradation and defect formation at higher La concentrations.

The EDS results (Table 1) suggest that the composition of the 0.02 La sample closely resembles that of the undoped sample. This suggests that, at low doping levels, La may participate in the structural modification of the sample, as also suggested by the first-principles calculations. Furthermore, EDS reveals a slight increase in Fe and a slight decrease in Se with increasing La content. This may be explained by the formation of La–Se (and to a smaller degree La–Te) compounds such as LaSe and La_2Se_3, which, however, were not observed by XRD yet may explain the particulates in SEM. The observed lattice parameter variation, together with the SEM and EDS results, suggests that La addition influences the structural and compositional evolution of $FeSe_{0.5}Te_{0.5}$. Previous studies have shown that the superconducting properties of Fe(Se,Te)-based materials are highly sensitive to compositional variations, which can simultaneously affect lattice parameters and electronic properties. In addition, local structural investigations of $FeSe_{1-x}Te_x$ have indicated that the local atomic environment may deviate from the average crystallographic structure [38, 39]. Furthermore, studies on doped FeSe systems have suggested that added elements may either participate in lattice modification or form secondary chalcogenide-related phases. Therefore, although the present results do not allow a direct determination of the exact atomic position of La, they indicate that La participates in the structural and compositional modification of the $FeSe_{0.5}Te_{0.5}$ matrix. Such modifications may contribute to the observed evolution of flux-pinning behavior and superconducting performance.

The temperature variation of magnetic moment (M–T) under H//c for all samples is presented in Fig. 6. Notably, the 0.04 La sample exhibits the lowest T_c, which may be associated with the nanoscale defects observed in SEM. The undoped and 0.08 La samples show a slightly broadened superconducting transition. The much narrower superconducting transition width and the larger magnetization observed for the 0.02 La sample indicate that the introduction of trace amounts of La enhances both the superconducting volume fraction and the homogeneity of the superconducting phase within the samples. In contrast, the superconducting volume fraction of the samples with higher La doping levels is lower than that of the undoped sample. The $x = 0.02$ sample exhibits the narrowest superconducting transition width, indicating relatively improved superconducting homogeneity and crystallinity. However, a narrower transition width does not necessarily correspond to a higher critical current density. While ΔT_c mainly reflects the uniformity of the superconducting phase, J_c is strongly influenced by the density and effectiveness of flux-pinning centers.

As shown in Fig. 7, there is a strong positive correlation between La content and *c*/*a* ratio, as well as strong negative correlations of La content to Se: Te ratio and T_c. Furthermore, Tc is positively correlated to Se/Te ratio and c/a ratio, which in turn is

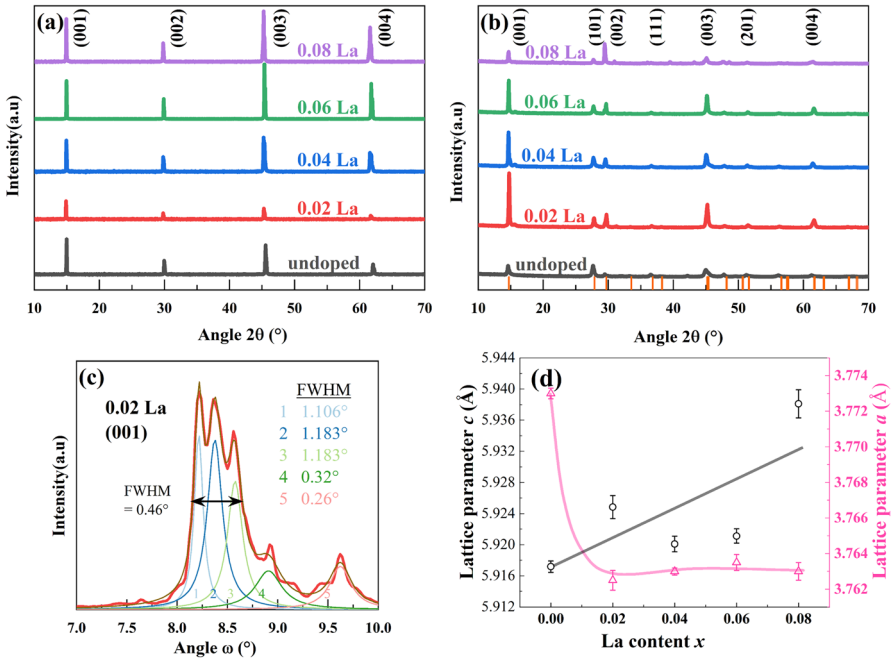

Fig.4 **a** XRD of the $La_xFe_{1-x}Se_{0.5}Te_{0.5}$ single crystals; **b** powder XRD of $La_xFe_{1-x}Se_{0.5}Te_{0.5}$ crystals. The XRD peaks match well with the tetragonal phases; **c** (001) rocking curve of the 0.02 La crystal; **d** lattice parameters of the $Fe_{1-x}Se_{0.5}Te_{0.5}$: La_x crystals as a function of the lanthanum level

negatively correlated to Se/Te ratio itself. A possible interpretation is that La doping strongly influences the *c*/*a* ratio both directly as well as via the Se: Te ratio (strong correlation between Se: Te and *c*/*a*), and influences T_c indirectly via the *c*/*a* ratio.

Figure 7a and b shows the isothermal magnetization hysteresis (M–H) loops of all samples at 6 K and 8 K for H∥c. The corresponding critical current density J_c shown in Fig. 7c and d can be calculated based on the Bean critical state model [40]:

$$J_{c,mag}\left[\frac{A}{\mathrm{cm}^2}\right]=\frac{20\frac{A\mathrm{cm}^2}{emu}\Delta\mathrm{M}\left[\frac{emu}{\mathrm{cm}^3}\right]}{a[cm]\left(1-\frac{a[cm]}{3b[cm]}\right)} \tag{8}$$

Here, $\Delta M = M_{down} - M_{up}$ (emu cm^{-3}) denotes the magnetization difference between the ascending (M_{up}) and descending (M_{down}) branches at a specific magnetic field. Parameters a (cm) and b (cm), where $a < b$, represent the width and length, respectively, of the crystal cross section normal to the applied field.

At both temperatures, the relatively lower J_c of the $x = 0.02$ sample may be associated with its improved crystallinity and reduced defect density. Although enhanced crystallinity favors superconducting homogeneity, it may simultaneously reduce the number of effective flux-pinning centers. In contrast, higher La concentrations introduce additional defect-related pinning centers, which enhance flux pinning and contribute to the observed increase in J_c.

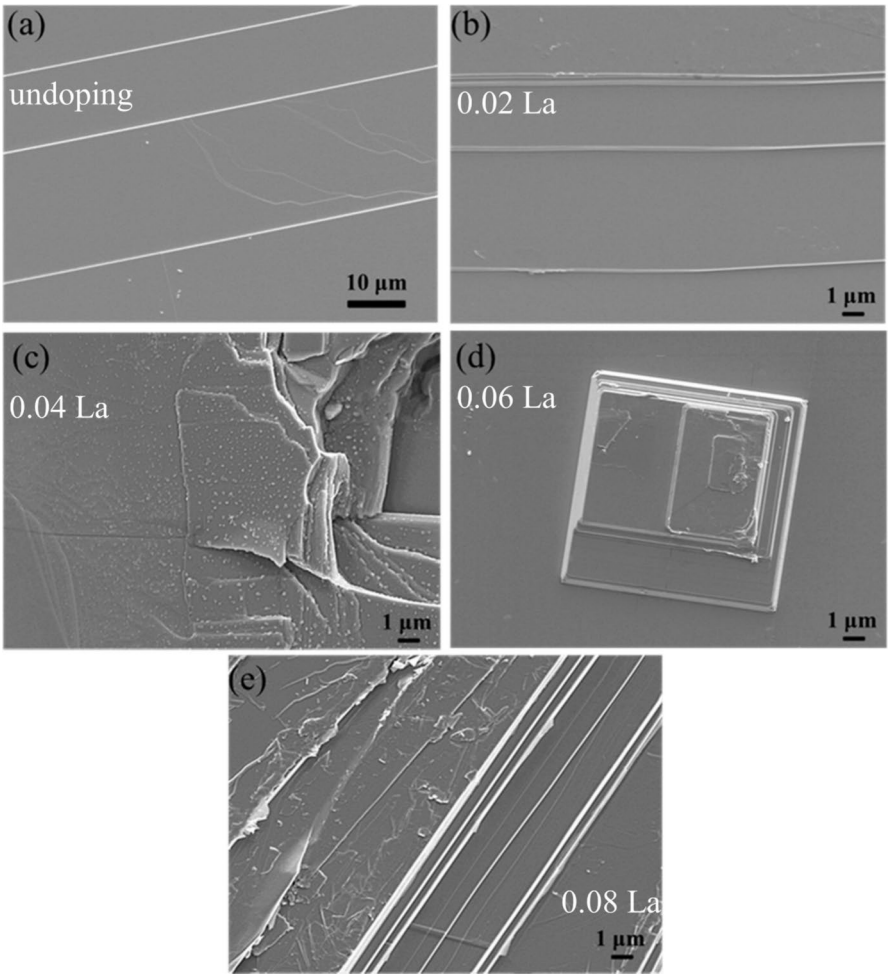

Fig.5 SEM images of **a** undoped; **b** 0.02 La; **c** 0.04 La; **d** 0.06 La; **e** 0.08 La sample

As shown in Fig. 8c and d, the second magnetization peak (SMP) is clearly visible in all samples. This indicates that multiple pinning mechanisms may exist in the sample, and the appearance of SMPs proves that the sample has undergone a transition from weak pinning mechanisms to strong pinning mechanisms [41, 42]. To further clarify the flux-pinning mechanism of La-doped samples, the normalized field dependence of pinning force density $F_{\mathrm{p}}=J_c\times \mathrm{B}$ was evaluated, while the Dew-Hughes model was employed to identify the dominant pinning centers. All data were normalized to the maximum value of the first peak for subsequent pinning mechanism analysis.

A scaling method, widely applied in high-temperature superconductors, was employed, defined by $h=H/H_{\mathrm{max}}$ and $f_p=F_{\mathrm{p}}/F_{\mathrm{p,\ max}}$, where H_{max} represents the

Table 1 EDS results of the element in La addition samples. The results have been scaled to $La_xFe_{1+\delta}Se_{1-x}Te_x$, where x is the nominal amount

sample	Nominal content			measured content		
	Fe	Se	Te	Fe	Se	Te
Undoped	1.00	0.5	0.5	1.00	0.47	0.53
0.02 La	0.98	0.5	0.5	1.01	0.46	0.54
0.04 La	0.96	0.5	0.5	1.02	0.49	0.51
0.06 La	0.94	0.5	0.5	1.07	0.43	0.57
0.08 La	0.92	0.5	0.5	1.05	0.43	0.57

magnetic field corresponding to the maximum of F_p [43]. The scaling of $f_p(h)$ is described by the following equations [44]:

$$f_p = \frac{9}{4}h(1-\frac{h}{3})^2 \tag{9}$$

$$f_p = \frac{9}{4}h^{1/2}(1-\frac{h}{5})^2 \tag{10}$$

$$f_p = 3h^2(1-\frac{2h}{3}) \tag{11}$$

Specifically, Eq. (9) is used for normal point pinning, Eq. (10) for surface pinning, and Eq. (11) for $\Delta\kappa$ pinning. The $f_p(h)$ curve of all samples can be described by Eq. (9) at low magnetic fields, whereas Eqs. (10) and (11) do not fit indicating that normal point pinning is the predominant pinning mechanism at low fields.

The evolution of the SMP with La addition suggests that the vortex-pinning environment is modified by La-induced structural disorder and local compositional variation. Similar SMP behavior has been reported in Fe-based superconductors and is generally associated with changes in vortex dynamics and the pinning landscape. Although the normalized pinning force curves are generally close to the theoretical behavior expected for normal point pinning, deviations from the ideal Dew-Hughes curves remain, especially in the high-field region. This indicates that the flux-pinning behavior cannot be fully described by a single pinning mechanism over the whole field range [45]. Similar results have been reported for $Ba_{0.6}K_{0.4}Fe_2As_2$and $YBa_2Cu_3O_{7-\delta}$ [17, 46]. Due to limitations in magnetic field testing, the pinning mechanism under high magnetic fields remains unclear. Further investigations into flux pinning under high magnetic fields will be conducted in the future. The different evolution trends of ΔT_c and J_c observed in the present work are consistent with recent studies on FeSe-based superconductors. Singh et al. reported that Pb addition in $FeSe_{0.5}Te_{0.5}$ can modify the microstructure, transport properties, and critical current density, indicating that chemical addition can affect superconducting performance through microstructural regulation [47]. Khan et al. further showed that the flux-pinning behavior of $FeSe_{0.5}Te_{0.5}$ is strongly dependent on magnetic field and pinning energy evolution [48]. In addition, Piperno et al. demonstrated that

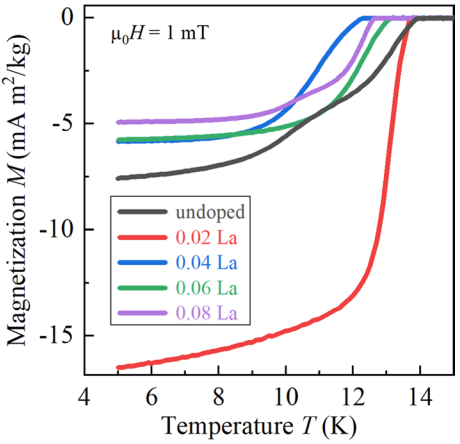

Fig.6 **a** M–T curves of the $Fe_{1-x}Se_{0.5}Te_{0.5}$: La_x single crystals with $H = 10$ Oe

high-performance Fe(Se,Te) films require optimized structural quality and flux-pinning conditions [45]. These studies suggest that superconducting transition sharpness and current-carrying capability may be governed by different microstructural factors. Therefore, the narrow ΔT_c observed in the $x = 0.02$ sample and the enhanced

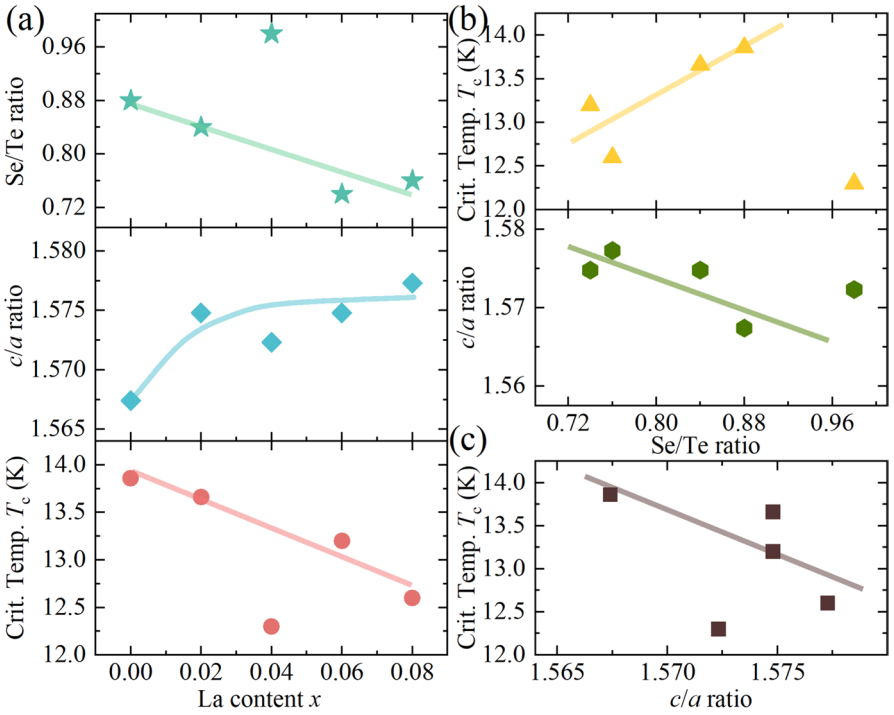

Fig.7 **a** Dependence of the T_c on x in the $La_yFeSe_{0.5}Te_{0.5}$ samples; **b** Se/Te with c/a and T_c parameters correlations; **c** c/a with T_c parameters correlations

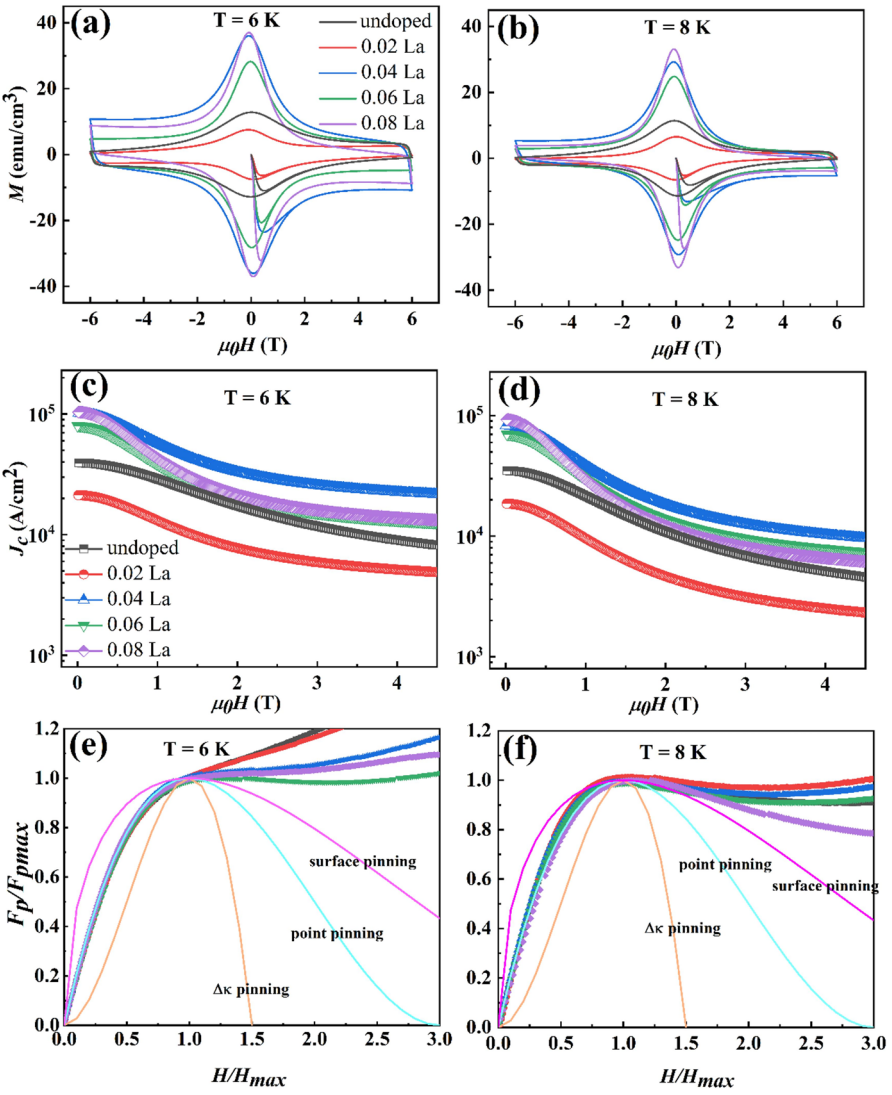

Fig. 8 Magnetization hysteresis loops of $Fe_{1-x}Se_{0.5}Te_{0.5}$: La_x for H//c at **a** $T = 6$ K and **b** $T = 8$ K. Critical current density (J_c) is shown in (**c**, **d**), while **e**, **f** display normalized pinning force density ($F_p/F_{p,\,max}$) versus reduced magnetic field (H/H_{max}). Solid lines in (**e**, **f**) correspond to fittings based on Eq. (2) for Δκ pinning (khaki), point pinning (blue), and surface pinning (pink)

J_c observed in the $x = 0.04$ sample are not contradictory, but rather reflect the balance between superconducting homogeneity and defect-assisted flux pinning.

Based on the combined experimental results and GPR-assisted trend analysis, the relatively favorable behavior of the $x = 0.02$ and $x = 0.04$ samples is reflected in different aspects. The $x = 0.02$ sample exhibits a sharper superconducting transition and stronger magnetic response in the M–T measurements, indicating improved

superconducting homogeneity. In contrast, the $x = 0.04$ sample shows the highest critical current density among the investigated compositions, suggesting enhanced flux-pinning performance. Therefore, the GPR results are used as a quantitative auxiliary analysis to support the experimental trends rather than as an independent determination of the optimal composition.

4 Conclusions

A series of La-doped $FeSe_{0.5}Te_{0.5}$ single crystals was synthesized through the self-flux method. La addition modifies the lattice parameters of $FeSe_{0.5}Te_{0.5}$, characterized by a decrease in lattice parameter a and a weak increasing tendency of lattice parameter c. La doping leads to an increase in the c-axis length, with La likely occupying positions between the (Se,Te) layers, preferably surrounded by Se. La addition lowers the superconducting transition temperature; however, tiny concentrations (0.02) seem to increase the superconducting volume fraction and sharpness of transition. La concentrations above 0.02, on the other hand, improve the critical current density, while the 0.04 La sample shows the highest values, which is likely related to the surface defects seen in that sample. The analysis of the pinning force densities revealed point pinning as the dominant pinning mechanism at low fields and a secondary magnetization peak (SMP) at all doping levels. At the same time, by combining this experiment with machine learning and utilizing GPR analysis, we further confirmed the evolution of superconducting and magnetic properties as a function of composition. The predicted results are consistent with experimental trends, suggesting that GPR can effectively capture La doping-dependent changes in T_c and magnetic susceptibility and provide useful guidance for future experimental design.

Acknowledgements This work was supported by Key Laboratory of materials and surface technology, Ministry of Education (No. xxx-2024-yb010).

Author Contributions J. Zhang created the idea and designed the study. J. Peng and S. Zhang discussed the data. Shunping Shi researched the literature. G. Yan and J. Hänisch revised and supervised the manuscript. Y. Zhao and C. Zhang provided the testing and preparation platform. All authors have approved the final version of the manuscript.

Funding Open Access funding enabled and organized by Projekt DEAL.

Data Availability No datasets were generated or analyzed during the current study.

Declarations

Conflict of interest The authors declare no competing interests.

References

1. E. Barbierato, A. Gatti, Electronics **13**, (2024)
2. M.A. Bessa, R. Bostanabad, Z. Liu, A. Hu, D.W. Apley, C. Brinson, W. Chen, W.K. Liu, Comput. Methods Appl. Mech. Eng. **320**, 633 (2017)
3. W. Wang, S. Feng, Z. Ye, H. Gao, J. Lin, D. Ouyang, Acta Pharm. Sin. B **12**, 2950 (2022)
4. F.-C. Hsu, J.-Y. Luo, K.-W. Yeh, T.-K. Chen, T.-W. Huang, P.M. Wu, Y.-C. Lee, Y.-L. Huang, Y.-Y. Chu, D.-C. Yan, M.-K. Wu, Proc. Natl. Acad. Sci. **105**, 14262 (2008)
5. M.H. Fang, H.M. Pham, B. Qian, T.J. Liu, E.K. Vehstedt, Y. Liu, L. Spinu, Z.Q. Mao, Phys. Rev. B **78**, 224503 (2008)
6. S. Margadonna, Y. Takabayashi, Y. Ohishi, Y. Mizuguchi, Y. Takano, T. Kagayama, T. Nakagawa, M. Takata, K. Prassides, Phys. Rev. B **80**, 064506 (2009)
7. K. Mukasa, K. Matsuura, M. Qiu, M. Saito, Y. Sugimura, K. Ishida, M. Otani, Y. Onishi, Y. Mizukami, K. Hashimoto, J. Gouchi, R. Kumai, Y. Uwatoko, T. Shibauchi, Nat. Commun. **12**, 381 (2021)
8. T.M. McQueen, Q. Huang, V. Ksenofontov, C. Felser, Q. Xu, H. Zandbergen, Y.S. Hor, J. Allred, A.J. Williams, D. Qu, J. Checkelsky, N.P. Ong, R.J. Cava, Phys. Rev. B **79**, 014522 (2009)
9. A. Leo, G. Grimaldi, A. Guarino, F. Avitabile, A. Nigro, A. Galluzzi, D. Mancusi, M. Polichetti, S. Pace, K. Buchkov, E. Nazarova, S. Kawale, E. Bellingeri, C. Ferdeghini, Supercond. Sci. Technol. **28**, 125001 (2015)
10. K.-W. Yeh, T.-W. Huang, Y. Huang, T.-K. Chen, F.-C. Hsu, P.M. Wu, Y.-C. Lee, Y.-Y. Chu, C.-L. Chen, J.-Y. Luo, D.-C. Yan, M.-K. Wu, EPL **84**, 37002 (2008)
11. R. Shipra, H. Takeya, K. Hirata, A. Sundaresan, Physica C **470**, 528 (2010)
12. A. Kumar, R. Tandon, V.P. Awana, IEEE Trans. Magn. **48**, (2012)
13. H.A. Alburaih, M.Z. Ansari, A.G. Abid, R.Y. Khosa, M.N. Ashiq, S. Manzoor, S. Aman, H. Chaudhry, M.S. Waheed, T.A. Taha, J. Sol-Gel Sci. Technol. **106**, 1 (2023)
14. M.Z. Cieplak, V.L. Bezusyy, Phil. Mag. **95**, 480 (2015)
15. S. Zhang, Y. Cui, Z. Wen, S. Li, Y. Zhao, Y. Chen, J. Supercond. Novel Magn. **36**, 1821 (2023)
16. N.V. Selezneva, A.S. Abouhaswa, E.V. Kislov, N.V. Baranov, Phys. Solid State **63**, 405 (2021)
17. R.F. Lopes, V.N. Vieira, A.P.A. Mendonça, F.T. Dias, D.L.D. Silva, P. Pureur, J. Schaf, J.J. Roa, J. Phys. Conf. Ser. **568**, 022014 (2014)
18. J. Zhang, Y. Luo, J. Hänisch, Y. Feng, X.S. Yang, D. Li, K. Zhao, H.Y. Zhou, Y. Zhao, J. Alloy. Compd. **999**, 174908 (2024)
19. M. Manasa, M. Azam, T. Zajarniuk, S. Stelmakh, T. Palasyuk, J. Mizeracki, T. Cetner, A. Morawski, C. Jastrzębski, M. Wierzbicki, A. Wiśniewski, S.J. Singh, (2024)
20. C.-M. Yang, P.-W. Chen, I.-G. Chen, X.-D. Qi, D.-C. Yan, M.-K. Wu, Supercond. Sci. Technol. **25**, 095010 (2012)
21. M. Manasa, M. Azam, T. Zajarniuk, R. Diduszko, J. Mizeracki, T. Cetner, A. Morawski, A. Wiśniewski, S.J. Singh, Ceram. Int. **50**, 714 (2024)
22. J. Zhao, Z. Wang, J. Alloy. Compd. **917**, 165358 (2022)
23. J. Liu, S. Zhang, M. Li, L. Sang, W. Zhao, Z. Li, Z. Cheng, L. Liu, B. Shao, J. Feng, C. Li, P. Zhang, S. Dou, X. Wang, L. Zhou, J. Alloy. Compd. **816**, 152683 (2020)
24. F. Kazemi, A. Özyüksel Çiftçioğlu, T. Shafighfard, N. Asgarkhani, R. Jankowski, Comput. Struct. **308**, 107657 (2025)
25. V.L. Deringer, A.P. Bartók, N. Bernstein, D.M. Wilkins, M. Ceriotti, G. Csányi, Chem. Rev. **121**, 10073 (2021)
26. P. Manfredi, IEEE Trans. Microw. Theory Techn. **71**, 2360 (2023)
27. N. Ulapane, K. Thiyagarajan, S. Kodagoda, in *2020 15th IEEE Conference on Industrial Electronics and Applications (ICIEA)* (2020), pp. 1154–1159
28. C.E. Rasmussen, C.K.I. Williams, *Gaussian Processes for Machine Learning* (The MIT Press, 2005)

29. A. Jain, S.P. Ong, G. Hautier, W. Chen, W.D. Richards, S. Dacek, S. Cholia, D. Gunter, D. Skinner, G. Ceder, K.A. Persson, APL Mater. **1**, 011002 (2013)
30. Materials Database Group, (2022)
31. Z. Deng, X. Hu, X. Lin, Y. Che, L. Xu, W. Guo, Energy **205**, 118000 (2020)
32. J. Xie, J. Huang, S.-H. Jiang, Y. Zhang, J. Meng, Geod. AI 100062 (2026)
33. S. Cao, S. Shen, L. Chen, S. Yuan, B. Kang, J. Zhang, J. Appl. Phys. **110**, 033914 (2011)
34. K.W. Yeh, C.T. Ke, T.W. Huang, T.K. Chen, Y.L. Huang, P.M. Wu, M.K. Wu, Cryst. Growth Des. **9**, 4847 (2009)
35. A.A.B. Baloch, S.M. Alqahtani, F. Mumtaz, A.H. Muqaibel, S.N. Rashkeev, F.H. Alharbi, Phys. Rev. Mater. **5**, 043804 (2021)
36. T.L. Ulrich, D.A. Lopes, T.L. Spano, A. Telles, A.E. Shields, J. Nucl. Mater. **625**, 156543 (2026)
37. S. Amira, D. Spångberg, M. Probst, K. Hermansson, J. Phys. Chem. B **108**, 496 (2004)
38. W. Guo, D. Jin, G.M. Seidel, H.J. Maris, Phys. Rev. B **79**, 054515 (2009)
39. K. Liu, Y. Li, J. Wang, Q. Ma, J. Li, X. Li, J. Alloys Compd. **647**, 41 (2015)
40. C.P. Bean, Phys. Rev. Lett. **8**, 250 (1962)
41. A. Galluzzi, K. Buchkov, V. Tomov, E. Nazarova, A. Leo, G. Grimaldi, A. Nigro, S. Pace, M. Polichetti, J. Phys. Conf. Ser. **1226**, 012012 (2019)
42. D. Dew-Hughes, Philos. Mag. J. Theor. Exp. Appl. Phys. **30**, 293 (1974)
43. T. Higuchi, S.I. Yoo, M. Murakami, Phys. Rev. B **59**, 1514 (1999)
44. L. Klein, E.R. Yacoby, Y. Yeshurun, A. Erb, G. Müller-Vogt, V. Breit, H. Wühl, Phys. Rev. B **49**, 4403 (1994)
45. L. Piperno, A. Vannozzi, A. Augieri, A. Masi, A. Mancini, A. Rufoloni, G. Celentano, V. Braccini, M. Cialone, M. Iebole, N. Manca, A. Martinelli, M. Meinero, M. Putti, A. Meledin, Sci. Rep. **13**, 569 (2023)
46. H. Yang, H. Luo, Z. Wang, H.-H. Wen, Appl. Phys. Lett. **93**, 142506 (2008)
47. S.J. Singh, R. Diduszko, P. Iwanowski, T. Cetner, A. Wisniewski, A. Morawski, Appl. Phys. A **128**, 476 (2022)
48. M.R. Khan, A. Leo, A. Nigro, A. Galluzzi, M. Polichetti, V. Braccini, M. Cialone, M. Scuderi, G. Grimaldi, Materials **14**, 5289 (2021)

Authors and Affiliations

Jie Zhang[1,2] · Jian Peng[1] · Jens Hänisch[3] · Shengnan Zhang[4] · Shunpeng Shi[1] · Chuanyu Zhang[1] · Fanggong Cai[5] · Guo Yan[6] · Yong Zhao[7]

✉ Jens Hänisch
jens.haenisch@kit.edu

[1] College of Physics, Chengdu University of Technology, Chengdu 610059, Sichuan, China

[2] School of Electrical Engineering, Southwest Jiaotong University, Chengdu 610031, China

[3] Institute for Technical Physics, Karlsruhe Institute of Technology, Hermann-von-Helmholtz-Platz 1, 76344 Eggenstein-Leopoldshafen, Germany

[4] Superconducting Materials Research Center, Northwest Institute for Nonferrous Metal Research, Xi'an 710016, China

[5] Key Laboratory of Materials and Surface Technology (Ministry of Education), School of Materials Science and Engineering, Xihua University, Chengdu 610039, Sichuan, China

[6] Western Superconducting Technologies Co., Ltd, Xi'an 710018, China

[7] College of Materials and Energy, Guang'an Institute of Technology, Guang'an 638000, China